



## Synthesis of $\text{SrFe}_x\text{Ti}_{1-x}\text{O}_3\text{-}\delta$ nanocubes with tunable oxygen vacancies for selective and efficient photocatalytic NO oxidation



Qian Zhang<sup>a</sup>, Yu Huang<sup>b,\*</sup>, Shiqi Peng<sup>a</sup>, Tingting Huang<sup>a</sup>, Jun-ji Cao<sup>b,\*</sup>, Wingkei Ho<sup>c</sup>, Shuncheng Lee<sup>d</sup>

<sup>a</sup> Key Laboratory of Aerosol Chemistry and Physics, Institute of Earth Environment, Chinese Academy of Sciences, Xi'an, 710061, China

<sup>b</sup> State Key Lab of Loess and Quaternary Geology (SKLLQG), Institute of Earth Environment, Chinese Academy of Sciences, Xi'an, 710061, China

<sup>c</sup> Department of Science and Environmental Studies, The Hong Kong Institute of Education, Hong Kong, China

<sup>d</sup> Department of Civil and Environmental Engineering, The Hong Kong Polytechnic University, Hong Kong, China

### ARTICLE INFO

#### Keywords:

Oxygen vacancies  
Fe substituted  $\text{SrTiO}_3$   
Photocatalysis  
Nitric oxide  
*In-Situ* DRIFTS

### ABSTRACT

Oxygen vacancies of metal oxides play critical roles in tuning activity and selectivity for many photocatalysis mediated reactions, yet the mechanism of NO oxidation on defect enriched photocatalyst surface is seldomly discussed. Herein, we provide detailed insight into the relationship between oxygen vacancy manipulation by extrinsic  $\text{Fe}^{3+}$  substitution in  $\text{SrTiO}_3$  host lattice and the photocatalytic performance of NO abatement. In particular, the hydrothermal synthesized  $\text{SrFe}_x\text{Ti}_{1-x}\text{O}_3\text{-}\delta$  nanocubes (denoted as SFTO-hyd sample) rather than the impregnated-post annealing sample, enabled oxygen vacancy formation, and promoted  $\text{O}_2$  adsorption and superoxide anion radicals ( $\text{O}_2^-$ ) formation. The SFTO-hyd ( $x = 5\%$ ) sample showed remarkably higher NO removal activity and selectivity under Xe lamp ( $\lambda > 420$  nm), in comparison with the pristine  $\text{SrTiO}_3$ , P25 and impregnation-doped SFTO sample, underlining the important roles played by coexisted  $\text{Fe}^{3+}$  sites and oxygen vacancies. The *in situ* diffuse reflectance IR spectroscopy (DRIFTS) mechanically revealed that  $\text{SrTiO}_3$  provided Lewis acidic sites for NO dark adsorption and photoreaction with nitrates as final products; the substitutional  $\text{Fe}^{3+}$  sites provided more active sites for NO adsorption and photoreaction with enhanced number of radicals. This study deepens the understanding of photocatalytic NO abatement on defective surface, and may also provide a simple and cost effective strategy for synthesizing efficient and selective photocatalysts for environmental remediation.

### 1. Introduction

Atmospheric  $\text{NO}_x$  at low concentration keeps promoting the reaction with volatile organic compounds to generate  $\text{O}_3$ , which brings about skin irritation and respiratory injury [1]. For high concentration  $\text{NO}_x$  gases from power plants and mobile vehicles, selective catalytic reduction and three way catalysis techniques are mainly employed [2]. But these control strategies are operated in high temperature conditions, which is energy inefficient and not suitable for purifying atmospheric  $\text{NO}_x$  at low level. Photocatalysis, by optical excitation of semiconductor materials to generate  $e^-/h^+$  pairs and reactive oxygen species (ROS), is proved to be a green and efficient process to remove  $\text{NO}_x$  from local environment [3–5]. For demonstration the European Life & project PhotoPAQ has carried out field studies in city tunnels, with results showing the effectiveness of photocatalytic  $\text{TiO}_2$  coatings for air purification [6]. In principle, the photo-oxidation removal of NO

is via the  $\text{NO} \rightarrow \text{NO}_2 \rightarrow \text{HNO}_2 \rightarrow \text{HNO}_3$  route [3], with  $\text{NO}_2$  being the most important toxic intermediate. Some visible light active photocatalysts with less positive valence band position, such as  $\text{g-C}_3\text{N}_4$ , is not oxidative adequate to transform NO completely, thereby generating  $\text{NO}_2$  in a large amount [7]. Given the high toxicity of  $\text{NO}_2$  (8 times more toxic than NO), it is very important to synthesize highly active and selective photocatalysts for NO removal [8].

Among various semiconductors,  $\text{SrTiO}_3$  with  $\text{ABO}_3$  perovskite structure is widely studied in photocatalysis, solar cells and electronics fields, owing to the excellent charge transport properties and chemical stability [9]. In particular, our previous studies have proved that  $\text{SrTiO}_3$  is effective for  $\text{NO}_x$  abatement [10,11]. The most attractive advantage of perovskite oxides is the flexible chemical composition by A- or B- site doping without structural collapse, by which one can manipulate the electronic states, optical and surface adsorption/reaction properties [12]. Recently, it has been reported that the chemical composition and

\* Corresponding author.

E-mail addresses: [huangyu@iecas.cn](mailto:huangyu@iecas.cn) (Y. Huang), [cao@loess.llqg.ac.cn](mailto:cao@loess.llqg.ac.cn) (J.-j. Cao).

crystal defects of photocatalysts impose great effects on activity and selectivity of NO conversion. For example, R. Sugrañez et al. found that the residual carbon in  $\text{Fe}_2\text{O}_3$  matrix enhanced the adsorption of  $\text{NO}_2$ , thereby providing sufficient time for complete oxidation [13]. Jonathan Z. Bloh et al. showed that the W/N co-dopants in  $\text{TiO}_2$  could remarkably induce a high selectivity for nitrate formation, but the mechanistic pathway is not elaborated [14]. Therefore, tuning surface composition and defects of perovskite  $\text{SrTiO}_3$ , and elaborating the effect on photocatalytic mechanism from molecular level are of crucial importance.

Among different types of defects, oxygen vacancies have been intensively studied in various photocatalytic reactions, such as  $\text{O}_2$  activation,  $\text{CO}_2$  reduction and  $\text{N}_2$  fixation [15–17]. Both experimental and theoretical evidences showed that surface oxygen vacancies provide active sites for strong chemisorption of gas molecules with lowered activation energy, thereby affecting the photocatalytic activity and product selectivity [15,18]. Especially,  $\text{O}_2$  molecules would preferably adsorb at oxygen vacancies, which also serve as trapping sites for photogenerated electrons, facilitate electron transfer to form superoxide radicals( $\text{O}_2^-$ ) and further boost photocatalytic reactions [19]. As one of the important reactive oxygen species,  $\text{O}_2^-$  is reported to have the longest lifetime (5 to hundreds of seconds) than other species, such as  $\cdot\text{OH}$  radicals (200  $\mu\text{s}$ ) and singlet oxygen (2  $\mu\text{s}$ ) [20]. Consequently, it is expected that boosting the number of  $\text{O}_2^-$  radicals would be advantageous for photocatalytic activity and selectivity enhancement.

To create oxygen vacancy defects,  $\text{NaBH}_4$  reduction and  $\text{H}_2$  heat treatment are commonly used [16,21]. But the surface oxygen vacancies are usually not sustainable under exposure of air for a long time. Recently, John. J. Carey et al. employed DFT to predict that the low valence cation substitution promotes the formation of oxygen vacancies in bulk  $\text{Cr}_2\text{O}_3$  with considerable reduced energy cost [22]. This is supposed to proceed more easily and facile in perovskite oxides due to their tolerable crystal structure. In order to create oxygen vacancies in  $\text{SrTiO}_3$ ,  $\text{Fe}^{3+}$  substitution at  $\text{Ti}^{4+}$  sites can be considered due to the lowered valence state, as a consequence, oxygen vacancy is formed to compensate for the negative charges. In addition, their similar ionic radii ensure the original crystal framework to be preserved [23]. Traditionally,  $\text{Cr}^{3+}$  is commonly chosen as dopant to increase the visible light activity. However, the natural abundance and eco-friendly property of iron make it more suitable for substitution. Furthermore, a series of contribution by Qingping Wu et al. has revealed that  $\text{Fe}^{3+}$  is a good adsorption site for NO molecule [24], which leads us to speculate how the activity and selectivity of NO photoreaction would be changed by  $\text{SrTiO}_3$  defect engineering with Fe substitution and rich oxygen vacancy formation.

Herein, we developed the hydrothermal approach to incorporate  $\text{Fe}^{3+}$  into  $\text{SrTiO}_3$  lattice instead of the conventional solid state reaction, and demonstrated the feasibility in comparison with the impregnation method. Comprehensive characterizations and DFT calculations proved the existence of oxygen vacancies induced by  $\text{Fe}^{3+}$  substitution. Compared with the bare  $\text{SrTiO}_3$  and P25, the SFTO-hyd samples displayed remarkably increased NO conversion efficiency and lowered production of  $\text{NO}_2$ . The Diffuse Reflectance Fourier Translation Infrared Spectroscopy (DRIFTS) revealed the key active sites in NO adsorption and transformation upon light. The aim of this study is to understand the effect of crystal defects on photocatalytic activity and selectivity of NO conversion, and to reveal the fundamental process by *in situ* IR spectroscopy. To the best of our knowledge, this is the first time that NO photocatalytic reaction mechanism over titanate perovskite is unveiled.

## 2. Experimental Section

### 2.1. Catalyst preparation

All chemicals were of analytical grade without further purification and purchased from Sinopharm Chemical reagent Co., Ltd, China. Oxygen vacancy enriched  $\text{SrTiO}_3$  was fabricated by  $\text{Fe}^{3+}$  substitution

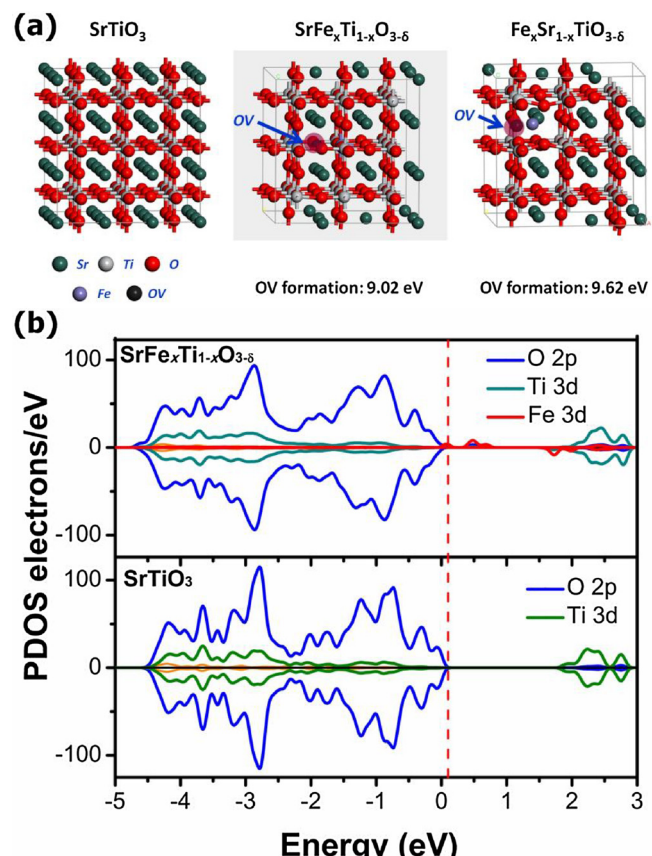


**Fig. 1.** (a) Crystal structures of  $\text{SrTiO}_3$ ,  $\text{SrFe}_x\text{Ti}_{1-x}\text{O}_3\delta$  and  $\text{Fe}_x\text{Sr}_{1-x}\text{TiO}_3\delta$ , and the OV formation energy for each case; (b) The density of states of  $\text{SrTiO}_3$  and  $\text{SrFe}_x\text{Ti}_{1-x}\text{O}_3\delta$ .

through a facile hydrothermal reaction. In a typical synthesis, 0.284 g TTIP and 0.211 g  $\text{Sr}(\text{NO}_3)_2$  were dissolved in 30 mL ethanol and 4 mL deionized water, respectively, and vigorously stirred for 30 min. The two solution were subsequently mixed and stirred for another 30 min, followed by adding 0.28 g NaOH with stirring for 1 h. The resultant was transferred into a 50 mL Teflon-lined autoclave and heated at 160 °C for 24 h. At last, the products were collected by centrifuged washing with deionized water and absolute ethanol for several times, and dried at 70 °C overnight. For  $\text{Fe}^{3+}$  substitution, a certain amount of  $\text{Fe}(\text{NO}_3)_3 \cdot 9\text{H}_2\text{O}$  (0.5, 1, 2, 5, 10% in molar ratio) was added in the precursor solution, with other conditions unchanged. The as-prepared samples were denoted as SFTO-hyd ( $x = 0.5, 1, 2, 5, 10\%$ , respectively). For comparison, the  $\text{SrFe}_x\text{Ti}_{1-x}\text{O}_3\delta$  sample was also prepared by the wet impregnation of as-prepared  $\text{SrTiO}_3$  with  $\text{Fe}(\text{NO}_3)_3 \cdot 9\text{H}_2\text{O}$  solution, and further calcined at 500 °C in air for 2 h. The as-obtained sample was denoted as SFTO-imp.

### 2.2. Characterization

The crystal structure of the as-prepared samples was analyzed by the PANalytical X'pert Pro powder X-ray diffractometer with a scanning rate of 0.017°  $\text{min}^{-1}$  ranging from 20° to 80° (PANalytical Corp., the Netherlands). X-ray photoelectron spectroscopy (XPS) were collected on ThermoFisher Scientific photoelectron spectrometer (Escalab 250Xi), with the sample being illuminated by monochromatic Al  $\text{K}\alpha$  X-ray source ( $\hbar\nu = 1486.71$  eV). All binding energies were calibrated by C 1 s at 284.8 eV as a reference. The chemical composition of  $\text{Fe}^{3+}$  in the bulk SFTO-hyd samples was characterized by an Agilent 725 ICP-OES instrument. Before measurement, the samples were pretreated with aqua regia to destroy organic matters. For morphology

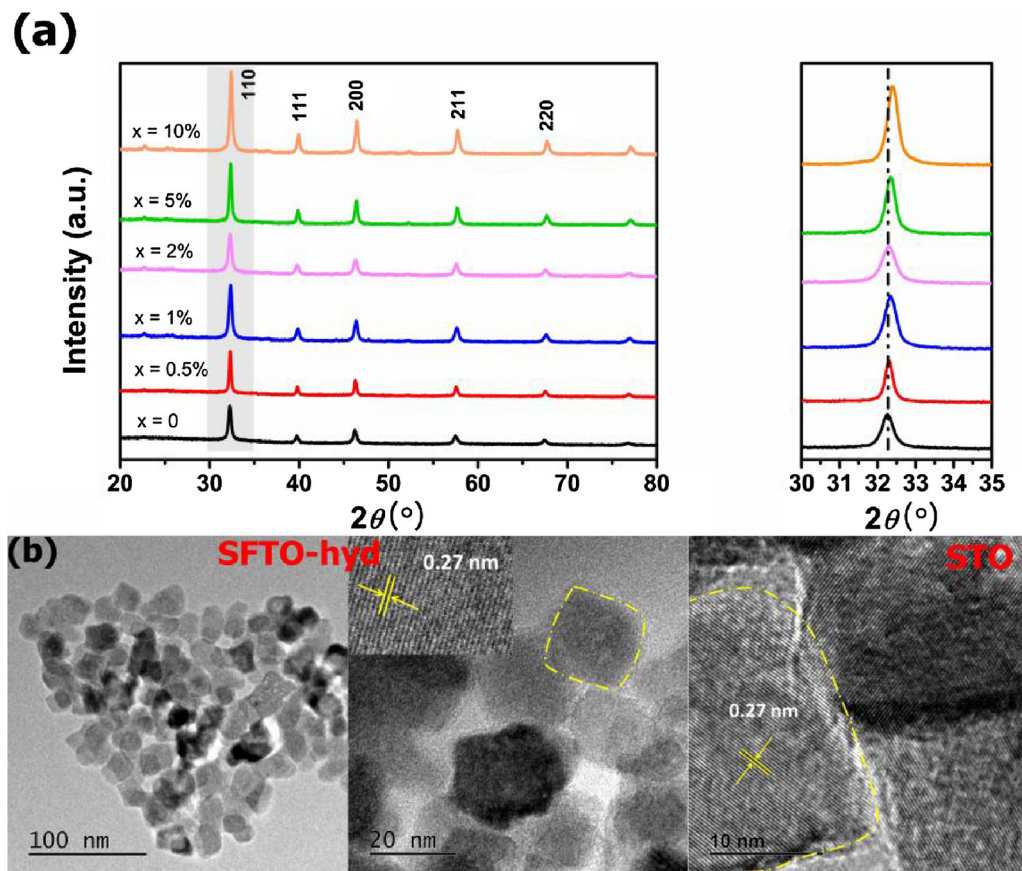


**Fig. 2.** (a) XRD pattern of SFTO-hyd samples at various Fe molar ratios; (b) TEM and HRTEM of pure STO and SFTO-hyd ( $x = 5\%$ ).

characterization, samples were ultrasonically dispersed in absolute ethanol and dropped onto the carbon coated copper grids, and then imaged on the JEM 3010 electron microscope at accelerating voltage of 200 kV (JEOL Corp., Japan). The optical property of the samples were investigated by measuring the UV-vis diffuse reflectance spectroscopy (UV-vis DRS) on the Agilent Cary 100 instrument (Agilent Corp., the United States) equipped with a integrating sphere, using  $\text{BaSO}_4$  reflection as a reference. The bandgap was calculated by converting the reflection into absorbance through Kubelka-Munk function. For oxygen vacancy characterization, electron spin resonance spectra recorded at 77 K were collected on a Bruker ER200-SRC instrument (Bruker Corp., Germany). The spectra were recorded at 100 kHz field modulation frequency, 0.1 mT field modulation amplitude and 9064.6 MHz microwave frequency. The Brunauer-Emmett-Teller surface area was determined by measuring the nitrogen adsorption-desorption isotherms at 77 K using a Micrometrics ASAP2020 equipment. Oxygen temperature programmed desorption ( $\text{O}_2$ -TPD) was carried out on a chemisorption analyzer (BJbuilder, PCA 1200, China), with powder samples of 50 mg supported on a frit in the continuous flow quartz reactor. Before  $\text{O}_2$  adsorption, the samples were pretreated under  $\text{N}_2$  at 300 °C for 30 min at heating rate of 10 °C min<sup>-1</sup>, to remove any surface contaminants. After the samples were cooled to room temperature,  $\text{O}_2$  at concentration of 100 ppm was flowed over the samples for 1 h. Once equilibrated, the pretreated sample was heated to 900 °C at a constant rate (8 °C min<sup>-1</sup>) under He flow (30 mL min<sup>-1</sup>). The desorption species were monitored using a thermal conductor detector. In order to probe the formation of superoxide  $\cdot\text{O}_2^-$  and hydroxyl  $\cdot\text{OH}$  radicals, ESR measurements of methanol-catalyst suspension were conducted on a Bruker ER200-SRC instrument (Bruker Corp., Germany) at room temperature. DMPO (5,5-dimethyl-l-pyrroline N-Oxide) was used as the spin trapping agent to detect the generation of radical adducts DMPO- $\cdot\text{OH}$  and DMPO- $\cdot\text{O}_2^-$ . The LED light at wavelength of 420 nm was used as excitation source

during ESR studies.

### 2.3. DFT calculation

All calculations were performed with the density functional theory (DFT) provided by the CASTEP program package, which employs the plane-wave basis sets to treat valence electrons and norm-conserving pseudo-potentials to approximate the potential field. Spin-polarized calculations were employed using the generalized gradient approximation (GGA) with the Perdew-Burke-Ernzerhof (PBE) to describe the exchange-correlation energy and electron interactions. A plane-wave cutoff energy of 450 eV with a  $3 \times 3 \times 3$  Monkhorst-pack  $k$ -point mesh was used for structure optimization and density of state (DOS) calculation. The geometries were not optimized until the energy, the force and the maximum displacement converged to  $2.0 \times 10^{-5}$  eV/atom,  $5 \times 10^{-2}$  eV/Å and  $2 \times 10^{-3}$  Å, respectively.

### 2.4. Photocatalytic NO removal

The evaluation of as-prepared photocatalysts was conducted in a continuous flow chamber with rectangular shape at dimension of 10 cm high, 30 cm long and 15 cm wide. Prior to irradiation, 0.1 g photocatalyst was immobilized on a petri dish situated in the chamber beneath the top quartz window for 5 cm, and a gas mixture of NO + air flow at a concentration of 400 ppb (3 L min<sup>-1</sup>) was accessed into the chamber. The mixture was produced by diluting NO feed stream (100 ppm) with zero air provided by a gas dilution calibrator (Sabio 4010, the United States). After the adsorption-desorption equilibrium was achieved, the 300 W electric input Xenon lamp (Perfectlight, microsolar300, Beijing) was turned on and the concentration of NO and  $\text{NO}_2$  was continuously monitored. Visible light ( $\geq 420$  nm) was obtained by passing light through the 420 nm cutoff filter and the optical

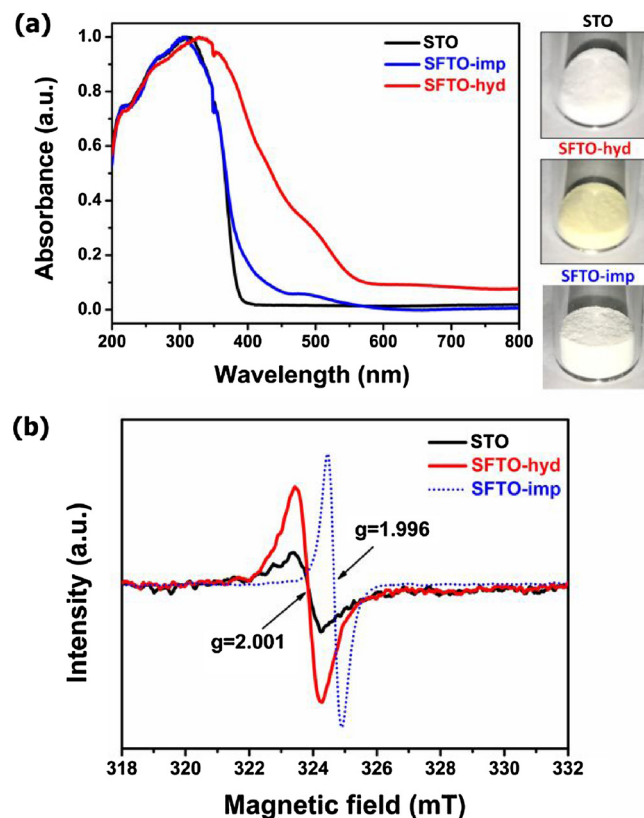


Fig. 3. (a) UV-vis diffuse reflectance spectra of the STO, SFTO-hyd ( $x = 5\%$ ) and SFTO-imp ( $x = 5\%$ ) samples, respectively. (b) EPR spectra of the pure STO, SFTO-hyd ( $x = 5\%$ ) and SFTO-imp ( $x = 5\%$ ) samples measured at 77 K.

power density reaching the sample surface was calibrated to be 28.93 mW/cm<sup>2</sup> (Thorlabs PM100D optical power meter). The whole measurement was conducted at ambient conditions and relative humidity of  $30 \pm 5\%$ . The removal efficiency of NO at any given time was denoted as  $C_{NO}/C_0$ , where  $C_{NO}$  is the NO concentration at given time, ppb; and  $C_0$  is the initial concentration of NO, ppb. The higher NO removal efficiency means that the as synthesized photocatalyst is more capable of decomposing air pollutant. NO<sub>2</sub> concentration was simultaneously recorded during the process, and we defined the NO<sub>2</sub> selectivity with the equation: NO<sub>2</sub> selectivity(%) = NO<sub>2</sub> yield / (C<sub>0</sub> - C<sub>NO</sub>).

### 2.5. DRIFTS for NO adsorption and conversion

The DRIFTS measurement was conducted on a Nicolet iS50FT-IR spectrometer (Thermo, USA) equipped with an *in situ* diffuse reflectance cell and a high temperature chamber. Photocatalyst was preheated in Ar to remove any surface adsorbates and then cooled to room temperature (25 °C). The IR spectrum of each pretreated catalyst was recorded and taken as the background reference, which was later subtracted from each spectrum. Then a gas mixture of NO + O<sub>2</sub> (flow rate 1:3; 8 mL/min vs. 24 mL/min) was purged into the DR cell for adsorption on the pretreated catalyst to mimick the real situation. After 30 min, the light (provided by the Xe lamp with a 420 nm cutoff filter) was turned on to initiate the photocatalytic reaction. The IR spectra were both collected during light on and off period in time sequence at each minute through a mercury-cadmium-telluride (MCT) detector.

## 3. Results and discussion

### 3.1. DFT calculations of oxygen vacancy formation and density of states

To figure out the origin of oxygen vacancy generation in SrTiO<sub>3</sub>

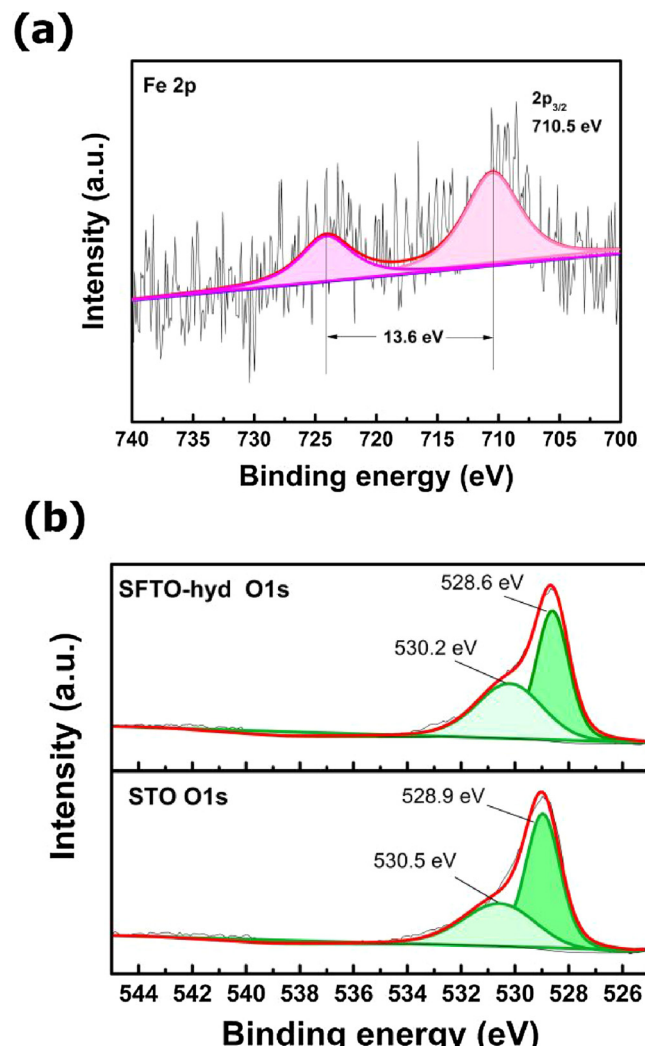


Fig. 4. High resolution XPS spectra of Fe 2p and O 1s orbitals in the SFTO-hyd ( $x = 5\%$ ) sample and the bare STO sample.

induced by Fe<sup>3+</sup> substitution, we employed the DFT calculation to analyze the defect formation energy [25]. SrTiO<sub>3</sub> belongs to the space group of *Pm3m* and has the lattice parameter of  $a = 3.98 \text{ \AA}$ . The  $2 \times 2 \times 2$  supercell is adopted to investigate the Fe substitution. There are two different substitution possibilities, with Fe replacing for Ti atom and Sr atom, respectively (Fig. 1a). To compare the relative stability of these two cases, the formation energy  $E_f$  of the substitutionally doped systems was estimated according to the following equation

$$E_f = E_{doped-O\ vacancy} + E_X + 1/2E_{O2} - E_{pure} - E_{Fe}$$

in which  $E_{doped-O\ vacancy}$  is the total energy of the SrTiO<sub>3</sub> containing the Fe atom and oxygen vacancy, and  $E_{pure}$  denotes the total energy of pure SrTiO<sub>3</sub> system.  $E_X$  is the energy of per Ti or Sr atom obtained from Ti and Sr bulk, respectively.  $E_{Fe}$  is the energy of per Fe atom in bulk model and  $E_{O2}$  is the energy obtained from O<sub>2</sub> molecule. When using a  $2 \times 2 \times 2$  supercell, the OV formation energy of Fe<sup>3+</sup> substituting for Ti<sup>4+</sup> site is 9.02 eV, while that substituting for Sr<sup>2+</sup> site is 9.62 eV. This suggests that oxygen vacancy is favorably generated by Fe replacement at Ti site due to their similar ionic radii (Fe<sup>3+</sup>: 0.79 Å; Ti<sup>4+</sup>: 0.75 Å), in line with the previous literature [26,27]. In the meantime, the conduction band (CB) and valence band (VB) structure of SrTiO<sub>3</sub> before and after Fe substitution were calculated and displayed in Fig. 1b. From the DOS diagram we can observe that for bare SrTiO<sub>3</sub> the top of valence band is dominated by O 2p orbitals, while the bottom of conduction band is mainly composed of Ti 3d orbitals. The bandgap is

**Table 1**

Element atomic concentration in each sample by XPS measurement.

Sample (nominal Fe content)	Fe 2p at. %	Ti 2p at. %	O 1s at. %	Calculated Fe: (Fe + Ti) ratio, %		Calculated Ti <sub>2p</sub> : O <sub>latt</sub> ratio	Calculated O <sub>surf</sub> : O <sub>latt</sub> ratio
				O 1s <sub>latt</sub>	O 1s <sub>surf</sub>		
STO	/	21.04	41.99	27.09	/	1.99	0.39
SFTO-hyd (x = 5%)	0.95	20.48	36.84	30.86	4.4	1.79	0.45
SFTO-imp (x = 5%)	0.35	16.47	35.75	17.53	2.0	2.17	0.32

approximately 1.8 eV, which is smaller than the experimental value mainly due to the restrictions of PBE method. As in the case of  $\text{SrFe}_x\text{Ti}_{1-x}\text{O}_3\delta$ , new band level extends from the O 2p and Ti 3d orbitals into the gap region, which reduces the bandgap value to about 1.2 eV. Therefore, it is speculated that  $\text{SrFe}_x\text{Ti}_{1-x}\text{O}_3\delta$  with increased oxygen vacancy density would be facile by visible light excitation.

### 3.2. Phase structure, morphological, optical and surface characteristics of photocatalysts

To verify the calculation results, we synthesized  $\text{SrFe}_x\text{Ti}_{1-x}\text{O}_3\delta$  samples through a facile hydrothermal method. The XRD patterns shown in Fig. 2a indicates that Fe substitution barely changes the main diffraction peaks as compared to the unmodified  $\text{SrTiO}_3$ , but the (110) peak exhibits tiny shift when the Fe addition level was increased to 10%. The peak slightly shifts to higher  $2\theta$  value, indicating *d*-spacing decrease and lattice contraction although the inserted  $\text{Fe}^{3+}$  ionic size (0.79 Å) is larger than  $\text{Ti}^{4+}$  (0.75 Å) [23,26]. Qingping Wu et al. attributed this phenomenon to the formation of oxygen vacancies that results in the lattice parameter decrease [27]. The cubic structure with space group of *Pm3m* was obtained according to the JCPDS file No. 35-0734[26]. As Fe atomic concentration increased up to 10%, strong diffraction peaks are still maintained without any detectable impurity phases. This suggests the good solubility of  $\text{Fe}^{3+}$  in the  $\text{SrTiO}_3$  crystal lattice, which is probably resulted from Fe replacement for Ti without remarkable lattice distortion. In addition, the average crystallite size of SFTO-hyd (x = 5%) was calculated to be 35 nm approximately through the Scherrer equation, as estimated from the strongest (110) diffraction peak at 32.5°. The TEM result provides consistent evidence that the average particle size of SFTO-hyd (x = 5%) is around 30 nm, and the sample is mainly consisted of rectangular nanoparticles. The HRTEM observation shows that both the unmodified  $\text{SrTiO}_3$  and SFTO-hyd samples exhibit (110) crystal plane with well-defined lattice fringes. The barely unchanged *d*-spacing value of 0.27 nm reveals that the  $\text{Fe}^{3+}$  addition did not interfere with the course of crystallization during the hydrothermal stage.

We further carried out the optical measurements to see the actual changes by Fe substitution and OV formation. Fig. 3a shows the normalized UV-vis diffuse reflectance spectra that the bare STO has a sharp absorption edge around 390 nm, corresponding to a bandgap transition of 3.25 eV using the Kubelka-Munk function. With increasing the  $\text{Fe}^{3+}$  content, the absorption band edge shows gradual shift towards longer wavelength which implies narrowed band gap (Fig. S2). For the SFTO-hyd (x = 5%) sample, the band edge position at 550 nm corresponds to the band gap of 2.75 eV. Moreover, an important feature to note is the absorption tail extending throughout the visible light region. As reported in previous literature, such band tail absorption (also called Urbach tail) is usually associated with existence of crystalline disorder/defects, more often indicating the generation of oxygen vacancies as shallow energy levels [19]. Consequently, the change in electronic structure of STO by Fe substitution leads to a color variation from white to faint yellow as photos indicate. William L. Harrigan et al. also assigned the coloration of  $\text{SrTiO}_3$  by  $\text{Cr}^{3+}$  doping to oxygen deficiency in their work [28]. On the other hand, we tested the Fe doped sample

prepared by the impregnation method. As one can notice that its absorption spectrum does not display the band tail absorption feature throughout visible, thus declaring the failure in generating oxygen vacancies. To provide more convincing evidence, we conducted the EPR measurement at 77 K with spectra shown in Fig. 3b. It is clear to see that the pristine STO shows a small symmetrical EPR signal at  $g = 2.001$ , which is typically ascribed to the electrons trapped on oxygen vacancies [15]. So it indicates that oxygen vacancies are already present on as-prepared STO. However, when Fe was added the signal becomes stronger, which illustrates the increased concentration of oxygen vacancies. Moreover, the absence of the asymmetric EPR signal at  $g = 1.98$  suggests there are no  $\text{Ti}^{3+}$  species formed [29,30]; this fact is also supported by the sharp Ti 2p orbital peaks with Gaussian distribution dictating  $\text{Ti}^{4+}$  existence (Fig. S1). More importantly, the OV number can be facilely tuned by modifying the concentration of Fe ( $\text{NO}_3$ )<sub>3</sub> precursor, which demonstrates a monotonous increase trend with the  $\text{Fe}^{3+}$  content (Fig. S2). In the case of the SFTO-imp sample, the spectrum displays a symmetrical signal at  $g = 1.996$  instead of 2.001, which is assigned to charge-uncompensated  $\text{Fe}^{3+}$  centers according to Michael Gratzel et al. [31] and Jinzhu Ma et al. [32]. Thereby, we suppose that the impregnated  $\text{Fe}^{3+}$  was not incorporated into the  $\text{SrTiO}_3$  lattice structure (Fig. S3), but probably forming tiny  $\text{Fe}_2\text{O}_3$  particles during post annealing stage. Based on the sensitive character of EPR to probe local environment, the above findings suggest that the hydrothermal method is more facile to introduce crystal defects within perovskite  $\text{SrTiO}_3$  lattice.

In order to quantitatively determine the chemical composition of Fe dopants in the SFTO-hyd samples, the ICP mass spectroscopy was conducted. For the SFTO-hyd samples with Fe molar ratio at 0.5, 1, 2, 5, 10%, their actual content in the bulk material are 0.7, 1.2, 2.4, 4.8, 9.5%, respectively. We further acquire the chemical composition and valence states by XPS characterization of the SFTO-hyd (x = 5%) sample (Fig. 4). XPS spectra provides accurate data for surface analysis within 4–5 nm range due to its surface sensitive character. The survey spectrum shows the presence of Sr, Ti, O, Fe elements and a trace amount of adventitious carbon (Fig. S1). Specifically, the Fe 2p orbital has doublet peaks at 710.5 eV and 724.1 eV, which are attributed to  $\text{Fe} 2p_{3/2}$  and  $\text{Fe} 2p_{1/2}$ , respectively. Besides, the splitting energy of 13.6 eV and the corresponding peak intensity ratio of 1:2 further confirm the +3 valence state of Fe ions [33]. With the aid of relative sensitivity factors (RSF) semi-empirical approach, we determined the atomic ratio of  $\text{Fe}^{3+}$  in the STO host. As summarized in Table 1, the practical Fe: (Fe + Ti) ratio in the SFTO-hyd sample is higher than that in the SFTO-imp sample, thereby suggesting that more  $\text{Fe}^{3+}$  cations were substituted for  $\text{Ti}^{4+}$  in the superfacial layer of  $\text{SrTiO}_3$ . Fig. 4 also shows the high resolution spectra of O 1s core level spectra of both samples, from which two peaks can be identified. For pure STO, the peak at 528.9 eV is believed as lattice oxygen (Ti-O-Ti), while the other located at 530.5 eV can be assigned to Ti-OH species. Table 1 shows that the percentage of hydroxyl group on SFTO-hyd (x = 5%) surface increases in comparison with STO, which is also a hint that more oxygen vacancies formed upon Fe substitution to facilitate water molecule adsorption and dissociation [34].

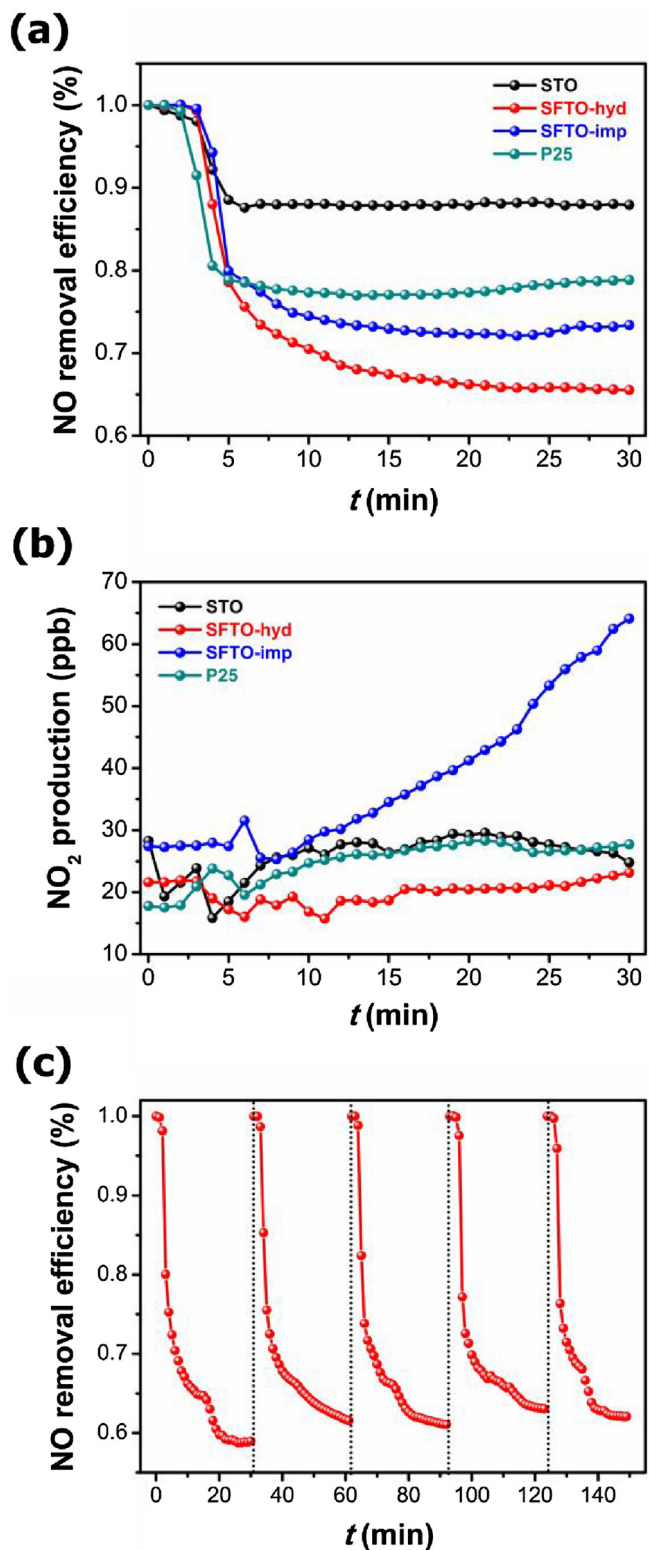


**Fig. 5.** (a) Time profile of NO photocatalytic removal with different photocatalysts under visible light irradiation ( $\lambda > 420$  nm), and the initial concentration of NO being 400 ppb; (b) NO<sub>2</sub> production as a function of time recorded simultaneously; (c) photostability measurements of the SFTO-hyd ( $x = 5\%$ ) sample in 5 reaction cycles.

### 3.3. Photocatalytic oxidation of NO under visible light irradiation and enhancement analysis

Photocatalytic oxidation profiles of NO with different samples were

recorded under 300 Xe lamp with a 420 nm cutoff filter. Before the light was turned on, 400 ppb level of NO was continuously fed into the reaction chamber loaded with samples and the whole system was maintained in the dark for 30 min to achieve adsorption/desorption equilibrium. As a control experiment, NO was not removed under visible irradiation in the absence of photocatalysts. In comparison, with STO and SFTO-hyd samples loaded, NO concentration drops sharply within the first 10 min before reaching a stable removal level; and the highest removal rate is achieved over the SFTO-hyd ( $x = 5\%$ ) sample (Fig. S4). This indicates that a 5% Fe(III) substitution level is more photoactive towards NO abatement. Furthermore, we compare the performance of SFTO-hyd ( $x = 5\%$ ) with SFTO-imp ( $x = 5\%$ ) and P25 samples under identical conditions shown in Fig. 5. It appears that SFTO-hyd still possesses the best photocatalytic activity for NO conversion during 30 min illumination, with 35% of initial NO being removed, which is much higher than SFTO-imp (25%) and P25 (20%) and the bare STO (15%). Meanwhile we monitored the change of NO<sub>2</sub> concentration over irradiation time with each photocatalysts. Fig. 5b shows that for pristine STO and SFTO-hyd ( $x = 5\%$ ) the generation of NO<sub>2</sub> are minimal during 30 min irradiation, which is in sharp contrast to SFTO-imp where NO<sub>2</sub> is continuously produced with time. The calculated NO<sub>2</sub> selectivity (Table S1 in SI) for SFTO-hyd is only 1.1%, further suggesting that SFTO-hyd is more efficient and selective for NO conversion to produce nitrates compared to other photocatalysts. Coincidentally Jinzhu Ma et al. also found that Fe doped TiO<sub>2</sub> prepared by the conventional impregnation method produced the highest amount of NO<sub>2</sub> [32]. It is possibly resulted from decreased surface area by post annealing when using the impregnation method. Hence, we conducted the BET surface area measurement of each catalyst and found out their surface area is quite similar (see Table S2). On this basis, we conclude that the improved activity and selectivity of the SFTO-hyd photocatalyst is due to the increased density of oxygen vacancies that facilitates visible light absorption, charge carrier generation and radical formation. Finally, we examined the performance of the SFTO-hyd sample in cyclic use and found that the NO removal efficiency was largely maintained, suggesting its relatively stable photocatalytic ability.

To understand the reason of photocatalytic performance enhancement, we investigated the effect of oxygen vacancies on charge carrier behavior by photocurrent measurement and the impedance spectroscopy. Fig. 6a shows that the SFTO-hyd ( $x = 5\%$ ) photoanode has fast response to light and higher photocurrent magnitude than the STO counterpart, which indicates that more charge carriers are generated and arrived at the surface for redox reaction. Moreover, according to the Nyquist plot of the impedance measurement (Fig. 6b), a small semicircle was developed for the SFTO-hyd sample, while an arc with large radius was found for the unsubstituted STO. Generally speaking, a Randles circuit model is employed to interpret the impedance result of semiconductor electrode, which is consisted of the electrolyte resistance in series with the parallel double layer capacitance and charge transfer resistance [35]. The smaller semicircle of SFTO-hyd sample illustrates that charge transfer resistance at the interface is decreased as a result of oxygen vacancy enrichment. Furthermore, to detect the reactive oxygen species involved in NO photocatalytic oxidation, we conducted the EPR spectroscopy using DMPO as spin trapping agent. A stable irradiation of methanol solution dissolved with samples for 15 min, respectively, caused the appearance of quartet peaks featuring 1:1:1:1 intensity, which are ascribed to the generation of free superoxide radicals ( $\cdot\text{O}_2^-$ ). Zhaohui Wang and coworkers briefly reviewed that  $\cdot\text{O}_2^-$  is facilely formed by one electron reduction of adsorbed O<sub>2</sub>, and more importantly to note, the oxygen vacancy is specific site for O<sub>2</sub> chemisorption [36]. Thereafter, the EPR spectra indicates that more  $\cdot\text{O}_2^-$  radicals are produced by Fe substitution and provide further evidence for oxygen vacancy formation. On the other hand, the EPR spectra display that the amount of hydroxyl radicals (OH) are also increased for the SFTO-hyd sample. This is consistent with the XPS result that more surface

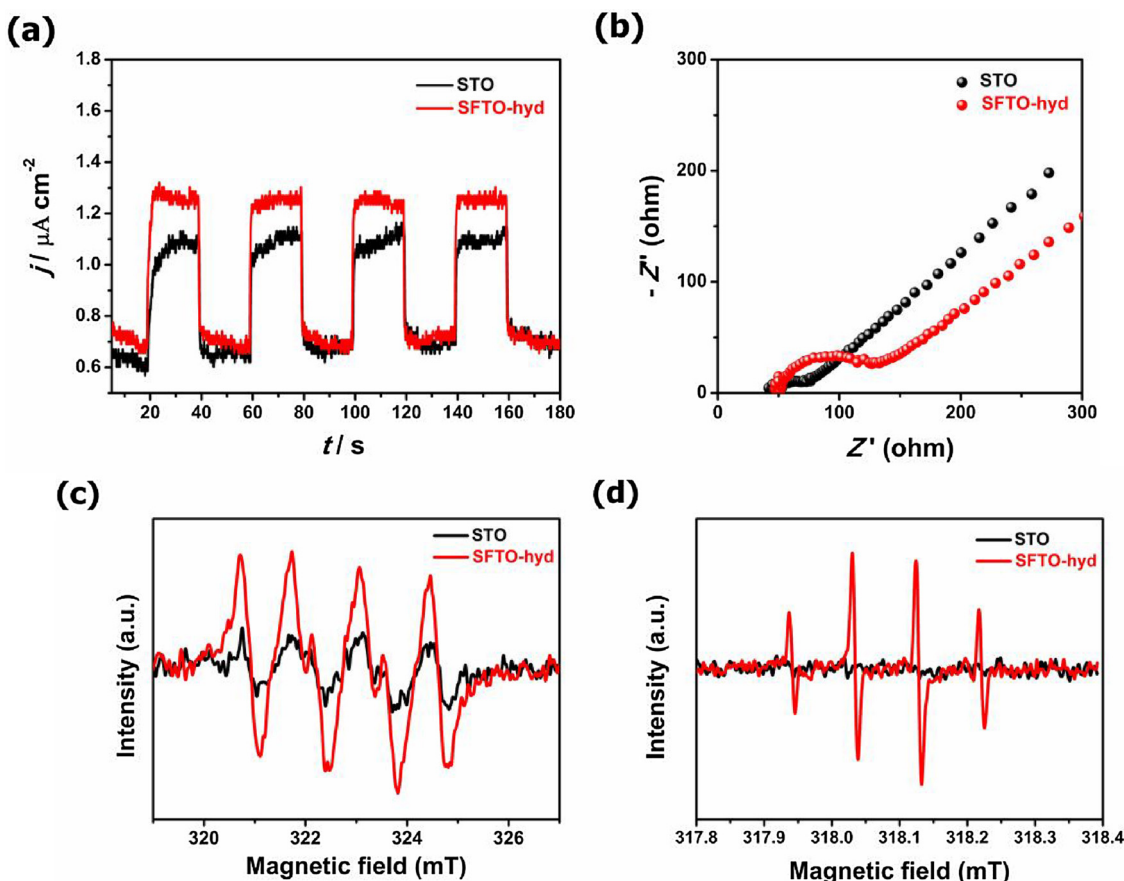


**Fig. 6.** (a) Photocurrent profile of the STO and SFTO-hyd ( $x = 5\%$ ) along with the LED irradiation ( $\lambda = 420 \text{ nm}$ ) on and off; (b) Nyquist plot of impedance spectroscopy at bias potential of  $0.2 \text{ V}$  in  $0.1 \text{ M} \text{Na}_2\text{SO}_4$  electrolyte; (c) and (d) EPR spectra of pure STO and SFTO-hyd ( $x = 5\%$ ) sample measured at R.T. after 15 min visible light irradiation, using DMPO as electron spin trapping agent.

hydroxyl groups on OV enriched SFTO-hyd sample would be facile to generate hydroxyl radicals by hole oxidation upon light irradiation.

In order to understand the effect of Fe(III) substitution level on photocatalytic performance, we also present the electrochemical measurements, EPR and  $\text{O}_2$ -TPD profile of various SFTO-hyd samples (Fe (III) level ranging from 0.5 to 10%) in the Supporting Information (Figs. S5 and S6). As expected, the optical absorption, OV number and radical concentration are all enhanced linearly with the increase of Fe(III) level in SFTO-hyd samples, however, the activity did not follow this trend. It is the SFTO-hyd ( $x = 5\%$ ) sample with the highest photocurrent density and facile charge transfer characteristics showed the best NO abatement performance. It appears that for the SFTO-hyd ( $x = 10\%$ ) sample, the charge recombination becomes predominant. This may result from the presence of superficial defects at high Fe doping levels after we analyzed the  $\text{O}_2$ -TPD spectra. The spectra (Fig. S6) show that the SFTO-hyd ( $x = 5\%$ ) displays an intense desorption peak at  $219 \text{ }^\circ\text{C}$ , while the other samples all exhibit desorption peaks around  $143 \text{ }^\circ\text{C}$  and  $308 \text{ }^\circ\text{C}$ . According to references [37] [38], oxygen desorption peaks below  $300 \text{ }^\circ\text{C}$  are classified as  $\alpha$ -oxygen, which indicates weakly bonded oxygen species at surface vacancies. Those peaks in the range of  $300 \sim 600 \text{ }^\circ\text{C}$  are denoted as  $\alpha'$ -oxygen, which can be ascribed to superficial lattice oxygen species. Finally, the desorption peaks higher than  $600 \text{ }^\circ\text{C}$  are denoted as  $\beta$ -oxygen;  $\beta$ -oxygen with sharp desorption profile usually corresponds to the reduction of some metal cations to a lower oxidation state ( $\text{Ti}^{4+}$  to  $\text{Ti}^{3+}$ ;  $\text{Fe}^{3+}$  to  $\text{Fe}^{2+}$ ), and comes from the bulk of the perovskite sample. Therefore, we conclude that the SFTO-hyd ( $x = 5\%$ ) sample with proper Fe composition possesses more surface oxygen vacancies, depressed charge recombination, and the best photocatalytic performance.

### 3.4. Photocatalytic mechanism via *in situ* diffuse reflectance FT-IR (DRIFTS) studies

To gain the reactive and intermediate species of NO on photocatalyst surface, the DRIFTS spectra were recorded in a Harrick cell filled by  $\text{NO} + \text{O}_2$  gas mixture, with and without irradiation for 30 min each. Before introducing target gas, the photocatalyst samples were pretreated with high purity Ar at elevated temperatures to remove any surface adsorbates. The correspondingly recorded spectra were set as baseline and deducted from all test spectra.

Without irradiation, the DRIFT spectra of STO (Fig. 7a) and SFTO-hyd ( $x = 5\%$ ) (Fig. 7b) both show pronounced bands at  $1259$  and  $1631 \text{ cm}^{-1}$  due to the N–O stretching vibration of bidentate nitrate (or bridging nitrate), and OH interacting with nitrate, respectively [39–42]. According to literature, surface nitroso species can be produced after  $\text{NO} + \text{O}_2$  coadsorption if samples possess Lewis acidity [39]. Moreover, the intensity of  $1259 \text{ cm}^{-1}$  band increases progressively with time, showing no saturation at 30 min. The result suggests that NO is more favorably stored as  $\text{NO}_3^-$  adsorbates on the surface of STO, which is consistent with the study reported by F.E. López-Suárez et al. that  $\text{ABO}_3$  perovskite exhibited high  $\text{NO}_x$  oxidation and storage capacity, and could be applied as potential NSR catalyst [43]. The other two samples with 1% and 10% Fe addition (Fig. S7a and b) also exhibit similar adsorption bands. Besides, new adsorption bands in the range of  $1456$ – $1575 \text{ cm}^{-1}$  appeared, indicating that  $\text{Fe}^{3+}$  serve as active sites for NO chemisorption, which is in good agreement with previous studies [44,45].

With irradiation turned on, the vibrations of nitrates at  $1259$ ,  $1631$  and  $1683 \text{ cm}^{-1}$  for both STO and SFTO-hyd ( $x = 5\%$ ) show no

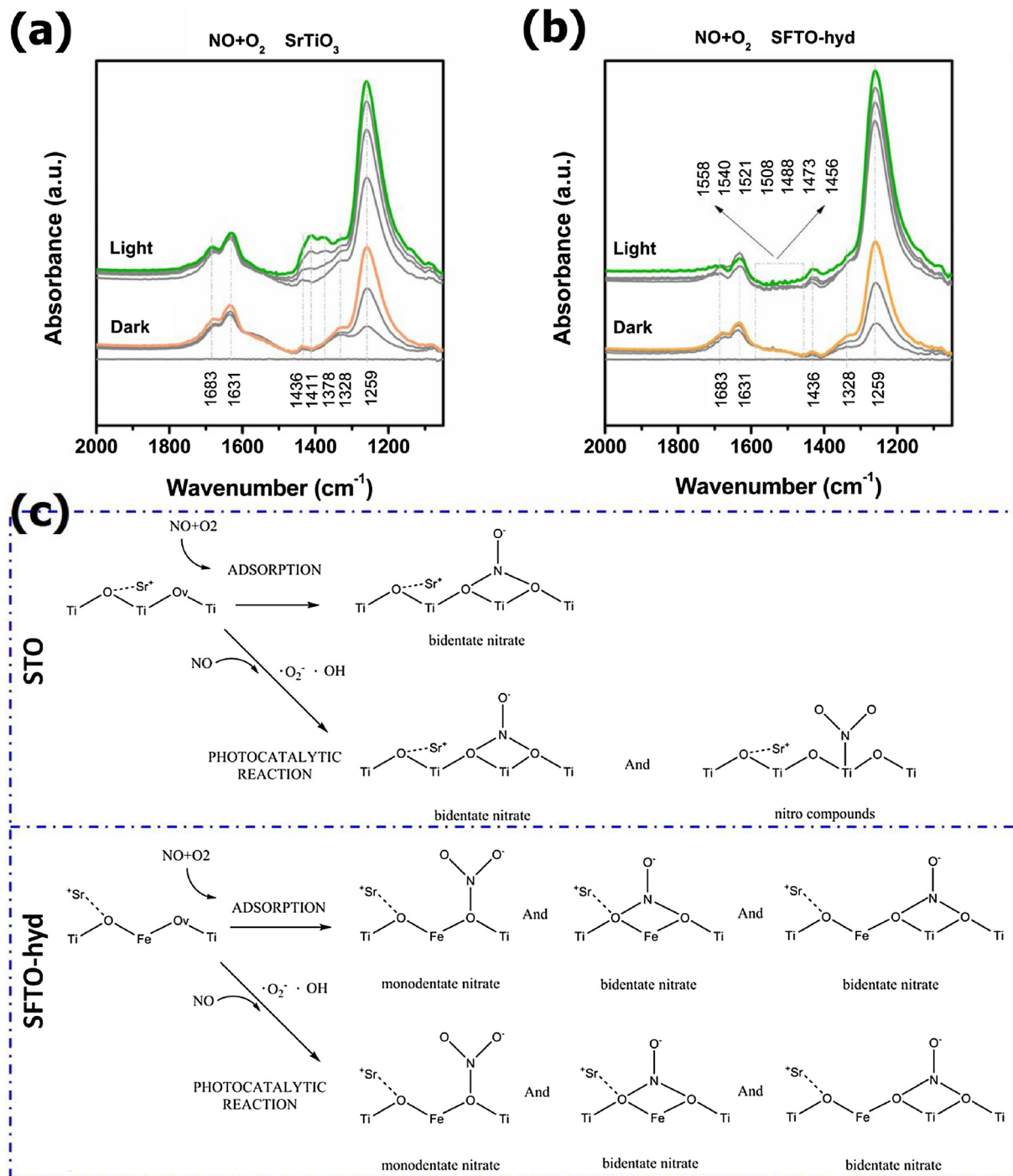


**Fig. 7.** Time dependent change in the DRIFTS spectra of  $\text{NO}$  and  $\text{O}_2$  mixture adsorbed on (a) bare  $\text{SrTiO}_3$  and (b) SFTO-hyd ( $x = 5\%$ ). The sample after gas adsorption was measured at  $25^\circ\text{C}$  under simulated solar light provided by Xe lamp; (c) Schematic diagram illustrating the photocatalytic oxidation of  $\text{NO}$  over STO and SFTO-hyd sample surface.

significant changes, except that the  $1259 \text{ cm}^{-1}$  band becomes stronger with time, suggesting that light promoted the generation of nitrate species. However, the spectra show distinct features in the range of  $1300\text{--}1600 \text{ cm}^{-1}$ . The addition of  $\text{Fe}^{3+}$  and exposure to light lead to the appearance of new adsorption bands at  $1456$ ,  $1473$ ,  $1488$ ,  $1508$ ,  $1521$ ,  $1540$  and  $1558 \text{ cm}^{-1}$ , which are owing to the stretching mode of monodentate or bidentate nitrate [40,42]. But the peaks at  $1436$ ,  $1411$ ,  $1378$  and  $1328 \text{ cm}^{-1}$  over the surface of STO become weakened or vanished for SFTO-hyd. These bands can be assigned to surface nitro groups [39,42,43]. Similar IR bands can be observed in the other two samples (Fig. S7a and b). Essentially, with the increase of  $\text{Fe}^{3+}$

substitution level, the bands ranging from  $1456\text{--}1600 \text{ cm}^{-1}$  become stronger, while those between  $1328$  and  $1436 \text{ cm}^{-1}$  get weakened. Based on the DRIFTS observations, we now conclude that  $\text{Fe}^{3+}$  provides more active sites for  $\text{NO}$  absorption and enhances the formation of  $\text{NO}_3^-$ -species, which explains the high activity and selectivity performance in photocatalytic  $\text{NO}$  conversion. In comparison, the IR adsorption signals associated with  $\text{NO}_3^-$  vibration are quite less for the bare  $\text{SrTiO}_3$ , which is in line with the low performance. In summary, we consider that the larger concentration of oxygen vacancies in SFTO-hyd leave more space for bidentate nitrate coordination both in the dark and under irradiation [44], and could be considered as potential photoassisted  $\text{NO}_x$

storage material.

#### 4. Conclusion

In conclusion, we investigated the photocatalytic NO abatement performance over the Fe-substituted STO nanocubes with tunable oxygen vacancies, and explored the adsorption and reaction mechanism by *in situ* DRIFTS technique. DFT calculation predicted, and EPR spectroscopy confirmed the existence of oxygen vacancies with tunable character in the SFTO-hyd samples. Upon visible light irradiation ( $\lambda > 420$  nm), the OV enriched SFTO-hyd samples exhibited more efficient and selective performance in NO abatement than the bare STO, P25 and SFTO-imp samples. It is analyzed that the superior photocatalytic activity and selectivity are mainly ascribed to enhanced surface oxygen vacancies and  $O_2$  adsorption, reduced electron transfer resistance and abundant reactive oxygen species (ROS) generation. Finally, the *in situ* DRIFTS study revealed that the OV enriched SFTO-hyd sample provided more active sites for NO adsorption, and contributed to enhanced NO conversion into nitrates under irradiation.

#### Acknowledgements

This research was financially supported by the National Natural Science Foundation of China (Grant No. 21707142), and the National Key Research and Development Program of China (Grant No. 2016YFA0203000). Yu Huang is also supported by the “Hundred Talent Program” of the Chinese Academy of Sciences.

#### Appendix A. Supplementary data

Supplementary material related to this article can be found, in the online version, at doi:<https://doi.org/10.1016/j.apcatb.2018.07.076>.

#### References

- S. Sillman, The relation between ozone,  $NO_x$  and hydrocarbons in urban and polluted rural environments, *Atmos. Environ.* 33 (12) (1999) 1821–1845.
- P. Granger, V.I. Parvulescu, Catalytic  $NO_x$  abatement systems for mobile sources: from three-way to lean burn after-treatment technologies, *Chem. Rev.* 111 (5) (2011) 3155–3207.
- J. Lasek, Y.H. Yu, J.C.S. Wu, Removal of  $NO_x$  by photocatalytic processes, *J. Photochem. Photobiol. C* 14 (1) (2013) 29–52.
- Y. Huang, Y.X. Gao, Q. Zhang, Y.F. Zhang, J.J. Cao, W.K. Ho, S.C. Lee, Biocompatible FeOOH-carbon quantum dots nanocomposites for gaseous  $NO_x$  removal under visible light: improved charge separation and high selectivity, *J. Hazard. Mater.* 354 (2018) 54–62.
- Y. Huang, D.D. Zhu, Q. Zhang, Y.F. Zhang, J.J. Cao, Z.X. Shen, W.K. Ho, S.C. Lee, Synthesis of a  $Bi_2O_3/CO_3/ZnFe_2O_4$  heterojunction with enhanced photocatalytic activity for visible light irradiation-induced NO removal, *Appl. Catal. B: Environ.* 234 (2018) 70–78.
- E. Boone, V. Akylas, F. Barmpas, A. Boréa, L. Bottalico, M. Cazaunau, H. Chen, V. Daëlle, T.D. Marco, J.F. Doussin, Construction of a photocatalytic de-polluting field site in the Leopold II tunnel in Brussels, *J. Environ. Manage.* 155 (2015) 136–144.
- G. Dong, L. Yang, F. Wang, L. Zang, C. Wang, Removal of nitric oxide through visible light photocatalysis by  $g\text{-}C_3N_4$  modified with perylene imides, *ACS Catal.* 6 (10) (2016) 6511–6519.
- M.E. Monge, B. D’Anna, C. George, Nitrogen dioxide removal and nitrous acid formation on titanium oxide surfaces—an air quality remediation process? *Phys. Chem. Chem. Phys.* 12 (31) (2010) 8991–8998.
- E. Grabowska, Selected perovskite oxides: Characterization, preparation and photocatalytic properties—a review, *Appl. Catal. B* 186 (2016) 97–126.
- Q. Zhang, Y. Huang, L.F. Xu, J.J. Cao, W.K. Ho, S.C. Lee, Visible-light-active plasmonic Ag–SrTiO<sub>3</sub> nanocomposites for the degradation of NO in air with high selectivity, *ACS Appl. Mater. Interfaces* 8 (2016) 4165–4174.
- Q. Zhang, Y. Huang, S.Q. Peng, Y.F. Zhang, Z.X. Shen, J.J. Cao, W.K. Ho, S.C. Lee, D.Y.H. Pui, Perovskite LaFeO<sub>3</sub>–SrTiO<sub>3</sub> composite for synergistically enhanced NO removal under visible light excitation, *Appl. Catal. B* 204 (2017) 346–357.
- R. Shi, G.I.N. Waterhouse, T. Zhang, Recent progress in photocatalytic  $CO_2$  reduction over perovskite oxides, *Sol. RRL* 1 (11) (2017), <https://doi.org/10.1002/solr.201700126>.
- R. Sugrañez, J. Balbuena, M. Cruz-Yusta, F. Martín, J. Morales, L. Sánchez, Efficient behaviour of hematite towards the photocatalytic degradation of  $NO_x$  gases, *Appl. Catal. B* 165 (165) (2015) 529–536.
- J. Bloh, A. Folli, D. Macphee, Photocatalytic  $NO_x$  abatement: why the selectivity matters, *RSC Adv.* 4 (86) (2014) 45726–45734.
- N. Zhang, X. Li, H. Ye, S. Chen, H. Ju, D. Liu, Y. Lin, W. Ye, C. Wang, Q. Xu, Oxide defect engineering enables to couple solar energy into oxygen activation, *J. Am. Chem. Soc.* 138 (28) (2016) 8928–8935.
- L. Liu, Y. Jiang, H. Zhao, J. Chen, J. Cheng, K. Yang, Y. Li, Engineering coexposed {001} and {101} facets in oxygen-deficient TiO<sub>2</sub> nanocrystals for enhanced  $CO_2$  photoreduction under visible light, *ACS Catal.* 6 (2) (2016) 1097–1108.
- H. Hirakawa, M. Hashimoto, Y. Shiraishi, T. Hirai, Photocatalytic conversion of nitrogen to ammonia with water on surface oxygen vacancies of titanium dioxide, *J. Am. Chem. Soc.* 139 (31) (2017) 10929–10936.
- Y. Ji, Y. Luo, New mechanism for photocatalytic reduction of  $CO_2$  on the anatase TiO<sub>2</sub>(101) surface: the essential role of oxygen vacancy, *J. Am. Chem. Soc.* 138 (49) (2016) 15896–15902.
- H. Li, J. Li, Z. Ai, F. Jia, L. Zhang, Oxygen vacancy-mediated photocatalysis of BiOCl: reactivity, selectivity and perspective, *Angew. Chem. Int. Ed.* 57 (1) (2017) 122–138.
- D. Wang, L. Zhao, H. Ma, H. Zhang, L.H. Guo, Quantitative analysis of reactive oxygen species photo-generated on metal oxide nanoparticles and their bacteria toxicity: the role of superoxide radicals, *Environ. Sci. Technol.* 51 (17) (2017) 10137.
- W. Zhou, W. Li, J.Q. Wang, Y. Qu, Y. Yang, Y. Xie, K. Zhang, L. Wang, H. Fu, D. Zhao, Ordered mesoporous black TiO<sub>2</sub> as highly efficient hydrogen evolution photocatalyst, *J. Am. Chem. Soc.* 136 (26) (2014) 9280–9283.
- J.J. Carey, M. Legesse, M. Nolan, Low valence cation doping of bulk Cr<sub>2</sub>O<sub>3</sub>: charge compensation and oxygen vacancy formation, *J. Phys. Chem. C* 120 (34) (2016) 19160–19174.
- T.H. Xie, X. Sun, J. Lin, Enhanced photocatalytic degradation of RhB driven by visible light-induced MMCT of Ti(IV)-O-Fe(II) formed in Fe-doped SrTiO<sub>3</sub>, *J. Phys. Chem. C* 112 (26) (2008) 9753–9759.
- Q. Wu, G. Mul, R.V.D. Krol, Efficient NO adsorption and release at  $Fe^{3+}$  sites in Fe/TiO<sub>2</sub> nanoparticles, *Energy Environ. Sci.* 4 (6) (2011) 2140–2144.
- J. Zhang, Z. Zhao, X. Wang, T. Yu, J. Guan, Z. Yu, Z. Li, Z. Zou, Increasing the oxygen vacancy density on the TiO<sub>2</sub> surface by La-doping for dye-sensitized solar cells, *J. Phys. Chem. C* 114 (43) (2010) 18396–18400.
- L.F.D. Silva, J.C. M’Peko, J. Andrés, A. Beltrán, L. Gracia, M.I.B. Bernardi, A. Mesquita, E. Antonelli, M.L. Moreira, V.R. Mastelaro, Insight into the effects of Fe addition on the local structure and electronic properties of SrTiO<sub>3</sub>, *J. Phys. Chem. C* 118 (9) (2014) 4930–4940.
- Q.P. Wu, Q. Zheng, R.V.D. Krol, Creating oxygen vacancies as a novel strategy to form tetrahedrally coordinated  $Ti^{4+}$  in Fe/TiO<sub>2</sub> nanoparticles, *J. Phys. Chem. C* 116 (2012) 7219–7226.
- W.L. Harrigan, S.E. Michaud, K.A. Lehuta, K.R. Kittilstved, Tunable electronic structure and surface defects in chromium-doped colloidal SrTiO<sub>3-δ</sub> nanocrystals, *Chem. Mater.* 28 (2) (2016) 430–433.
- Y. Xu, C. Zhang, L. Zhang, X. Zhang, H. Yao, J. Shi, Pd-catalyzed instant hydrogenation of TiO<sub>2</sub> with enhanced photocatalytic performance, *Energy Environ. Sci.* 9 (7) (2016) 2410–2417.
- X. Yu, B. Kim, K.K. Yu, Highly enhanced photoactivity of anatase TiO<sub>2</sub> nanocrystals by controlled hydrogenation-induced surface defects, *ACS Catal.* 3 (11) (2013) 2479–2486.
- M. Graetzel, R.F. Howe, Electron paramagnetic resonance studies of doped titanium dioxide colloids, *J. Phys. Chem.* 94 (6) (1990) 2566–2572.
- J. Ma, H. He, F. Liu, Effect of Fe on the photocatalytic removal of  $NO_x$  over visible light responsive Fe/TiO<sub>2</sub> catalysts, *Appl. Catal. B* 179 (1) (2015) 21–28.
- J.F. Moulder, J. Chastain, R.C. King Jr, Handbook of X-ray photoelectron spectroscopy: a reference book of standard spectra for identification and interpretation of XPS data, *Chem. Phys. Lett.* 220 (1) (1992) 7–10.
- S. Wu, J. Xiong, J. Sun, Z.D. Hood, W. Zeng, Z. Yang, L. Gu, X. Zhang, S.Z. Yang, Hydroxyl-dependent evolution of oxygen vacancies enables the regeneration of BiOCl photocatalyst, *ACS Appl. Mater. Inter.* 9 (19) (2017) 16620–16626.
- J.E.B. Randles, Kinetics of rapid electrode reactions, *Discuss. Faraday Soc.* 1 (1947) 11–19.
- Z. Wang, W. Ma, C. Chen, H. Ji, J. Zhao, Probing paramagnetic species in titanias-based heterogeneous photocatalysis by electron spin resonance (ESR) spectroscopy—a mini review, *Chem. Eng. J.* 170 (2–3) (2011) 353–362.
- Q.J. Meng, W.L. Wang, X.L. Weng, Y. Liu, H.Q. Wang, Z.B. Wu, Active oxygen species in  $La_{n+1}Ni_xO_{3n+1}$  layered perovskites for catalytic oxidation of toluene and methane, *J. Phys. Chem. C* 120 (2016) 3259–3266.
- S. Kaliaguine, A. Van Neste, V. Szabo, J.E. Gallot, M. Bassir, R. Muzychuk, Perovskite-type oxides synthesized by reactive grinding Part I. Preparation and characterization, *Appl. Catal. A Gen.* 209 (2001) 345–358.
- K. Hadjiiivanov, Identification of neutral and charged  $N_xO_y$  surface species by IR spectroscopy, *Catal. Rev.* 42 (1–2) (2000) 71–144.
- N. Liu, X. Chen, J. Zhang, J.W. Schwank, DRIFTS study of photo-assisted catalytic CO + NO redox reaction over CuO/CeO<sub>2</sub>-TiO<sub>2</sub>, *Catal. Today* 258 (2015) 139–147.
- M.A. Debeila, N.J. Coville, M.S. Scurrell, G.R. Hearne, The effect of calcination temperature on the adsorption of nitric oxide on Au-TiO<sub>2</sub>: drifts studies, *Appl. Catal. A* 291 (1–2) (2005) 98–115.
- J.C.S. Wu, Y.T. Cheng, In situ FTIR study of photocatalytic NO reaction on photocatalysts under UV irradiation, *J. Catal.* 237 (2) (2006) 393–404.
- F.E. López-Suárez, M.J. Illán-Gómez, A. Bueno-López, J.A. Anderson,  $NO_x$  storage and reduction on a SrTiCuO<sub>3</sub> perovskite catalyst studied by operando DRIFTS, *Appl. Catal. B* 104 (3–4) (2011) 261–267.
- Q. Wu, C.C. Yang, R.V.D. Krol, A dopant-mediated recombination mechanism in Fe-doped TiO<sub>2</sub> nanoparticles for the photocatalytic decomposition of nitric oxide, *Catal. Today* 225 (8) (2014) 96–101.
- A.R. Beltramone, O.A. Anunziata, Nature and reactivity of the active species formed after NO adsorption and NO +  $O_2$  coadsorption on an Fe-containing zeolite, *Catal. Lett.* 92 (3–4) (2004) 131–140.